Internal Oscillations in Tropical Mesoscale Convective Clusters

Bolei Yang[1,2], William R. Boos[2] and Ji Nie[1]

1. Department of Atmospheric and Oceanic Sciences, School of Physics, Peking University, Beijing, China

2. Department of Earth and Planetary Science, University of California, Berkeley, Berkeley, California

Corresponding author: Ji Nie

Email: jinie@pku.edu.cn

Bolei Yang: blyang@pku.edu.cn

William R. Boos: William.boos@berkeley.edu

This is a non-peer reviewed paper, which has been submitted to 'Journal of the atmospheric sciences.'

Abstract

In real-world observations, long-lived tropical mesoscale convective clusters (TMCCs) often exhibit quasi-periodic oscillations. Previous studies have suggested that these oscillations can be induced by external forcings. However, many idealized simulations provided evidence that TMCCs can display quasi-periodic behavior even without external forcings. Through this study, it is demonstrated that all TMCCs possess an inherent internal oscillation, and the physics behind is a convectively coupled inertia-gravity oscillation. When deep convection within a TMCC decays, the stratiform heating within the system triggers an inertia-gravity oscillation. This oscillation induces upward motion at lower levels of the disturbance, which facilitates the recovery of low-level buoyancy and initiates new convection. Notably, in this oscillation, diabatic heating serves not only as a consequence of the preceding oscillation but also as the source for the subsequent oscillation. The internal oscillation acts as a fundamental component in the life cycle of long-lived TMCCs, providing clearer physical intuition for understanding the variation of TMCCs in real-world scenarios.

1. Introduction

Mesoscale convective clusters are frequently observed in Earth's tropical regions. These clusters typically encompass systems like mesoscale convective systems, tropical depressions, tropical cyclones (TCs), and monsoon low-pressure systems (LPSs), with sizes ranging from hundreds to thousands of kilometers. These convective systems not only play a crucial role in the water and energy cycles within the tropics, but also significantly impact our social and economic activities (e.g., Nesbitt et al. 2000; Emanuel 2018; Houze 2018). However, the mechanisms driving the evolution of these systems remain unclear.

In real-world observations and numerical simulations, long-lived tropical mesoscale convective clusters (TMCCs) often interact with external forcings and demonstrate significant periodic characteristics. A typical example is the occurrence of large-scale, westward-propagating convective disturbances with periods of approximately 2 days in the equatorial western Pacific (e.g., Takayabu 1994; 1996). Studies indicate that this 2-day period of convection primarily results from the forcing of equatorial waves with wavelengths of around 2000 to 4000 km (e.g., Haertel and Johnson 1998; Wheeler et al. 2000; Haertel and Kiladis 2004). Another example is the diurnal cycle of convection over the tropical ocean. In the nighttime, the absence of shortwave heating cools the troposphere, which fosters convection by increasing relative humidity and enhancing convective instability. Conversely, convection is inhibited during the daytime due to strong shortwave heating (e.g., Gray and Jacobson 1977; Fingerhut 1978). This convective diurnal cycle is robust in nearly all types of TMCCs, particularly in those with longer lifetimes, such as TCs (e.g.; Browner et al. 1977; Dunion et al. 2014; Wu et al. 2014).

However, in many idealized simulations without external forcing, TMCCs also exhibit pronounced oscillations. For instance, in many idealized TC genesis simulations, which lack both the diurnal insolation cycle and lateral boundary forcing, significant oscillations of the disturbance can often be observed (e.g., Nolan 2007; Nicholls and Montgomery 2013; Yang and Tan 2020). Some studies suggest that this oscillation may be a model artifact resulting from the usage of double periodic boundary conditions, wherein gravity waves can return to their source and trigger new convection (e.g., Nolan, 2007). Nonetheless, in simulations with very large domains or damping lateral boundary conditions, the oscillation of the TC disturbances still occur (e.g., Li et al. 2006; Nicholls 2015). Similarly, oscillations of the convective disturbance can also be observed in idealized simulations of monsoon LPSs (e.g., Diaz and Boos, 2021a, b). These results show evidence that the oscillations of TMCCs are not solely attributable to external forcing, but may also be internally generated.

The aim of this work is to determine whether a TMCC exhibits internal oscillations and, if so, to identify the mechanisms underlying the oscillations. The rest of the paper is organized as follows: Section 2 introduces the simulation setups. Section 3 briefly analyzes the internal oscillation in full-physics simulations. Section 4 shows the critical role of low-level buoyancy in determining the precipitation. Section 5 reveals that the inertia-gravity oscillation is responsible for the oscillation of low-level buoyancy and precipitation. Finally, Section 6 offers a discussion and summary.

2. Methods

In this work, we use idealized numerical simulations to investigate the internal oscillations of TMCCs. The numerical model employed is the WRF version 4.6.0 (Skamarock et al., 2019). The model domain extends to an altitude of 27 km, with the upper third consisting of a sponge layer. There are 50 vertical levels, with 10 levels located below 1 km height. The initial sounding is derived from Jordan (1958), which is a typical tropical sounding commonly used in simulations.

The simulations cover a horizontal domain size of 1800 km × 1800 km, with a horizontal resolution of 3km. To rule out the effects of gravity waves propagating back to their sources, it is better to use open lateral boundary conditions. However, adopting open lateral boundary condition leads to a drastic drying of the domain, with the domain-mean moisture content decreases by 40% in the first 3 days. Therefore, we still use doubly periodic lateral boundary condition, but add a sponge layer at the lateral boundaries of the domain (e.g., Li et al., 2006). This sponge layer is 180 km wide at the lateral boundaries, with the diffusion coefficient set to 1000 times the model's predicted value. The simulations maintain a fixed sea surface temperature SST of 302.15 K and a constant solar radiation of 350 W m^{-2}. The Thompson microphysics scheme (Thompson et al., 2004) and the RRTMG radiation scheme (Iacono et al. 2008) are implemented in our simulations. The boundary layer scheme is YSU, coupled with the revised Monin–Obukhov surface-layer scheme (Hong et al. 2006).

All simulations initiate with a moist bubble centered in the domain. The moisture bubble has a radius of 150 km and a height of 3 km, with the water vapor mixing ratio set at 110% of the initial sounding value. We conduct three simulations with Coriolis forces set to 10^{-4} s^{-1} (CTLF10), 5×10^{-5} s^{-1} (CTLF05) and 0 s^{-1} (CTLF0), respectively (Table 1). All the simulations are run for 72 hours, and results are output every 2 hours. In the following analysis, we will mainly focus on the results in CTLF10, and the results in the other two experiments will be briefly compared.

Table 1 Descriptions of experiments.

Name	**Description**
CTLF10	An 1800 km×1800 km full-physics simulation with Coriolis parameter set to be 1×10^{-4} s^{-1}. The lateral boundary condition is double periodic, with a damping layer of 180 km wide.
CTLF05	As CTLF10, with Coriolis parameter set to be 5×10^{-5} s^{-1}.
CTLF0	As CTLF10, without Coriolis force.
Dry2_F10	A 3000 km×3000 km simulation forced with a stratiform heating profile, without microphysics and radiation parameterization. The open lateral boundary condition is used. The other settings are with CTLF10.
Dry2_F05	As Dry2_F10, with Coriolis parameter set to be 5×10^{-5} s^{-1}.
Dry2_F0	As Dry2_F10, without Coriolis forcing.
Dry1_F10	As Dry2_F10, forced with a deep convective heating profile.
Dry1_F05	As Dry1_F10, with Coriolis parameter set to be 5×10^{-5} s^{-1}.
Dry1_F0	As Dry1_F10, without Coriolis force.

3. Internal oscillation of TMCCs

The time series of the precipitation rate in the disturbance region of the three simulations are shown in Fig. 1a. All three simulations exhibit significant oscillations.

Specifically, the periods in CTLF10, CTLF05 and CTLF0 are around 15 hours, 18 hours and 30 hours, respectively, indicating a noticeable increase in the period as the Coriolis parameter decreases.

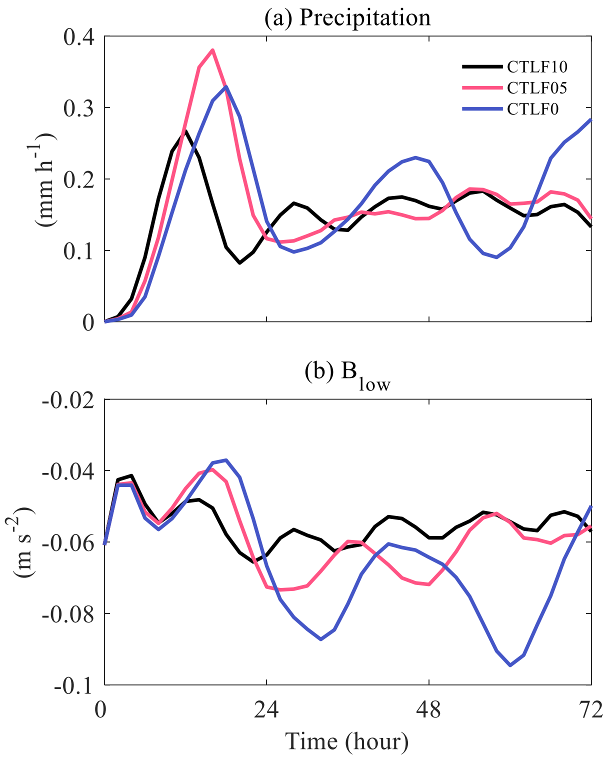

Fig.1 Time series of (a) precipitation (mm h^{-1}) and (b) low-level buoyancy (m s^{-2}) over the inner 150 km radii of the disturbance in CTLF10 (black), CTLF05 (red), and CTLF0 (blue).

To further confirm that this oscillation is physically meaningful rather than a result of model noise, we present the time-height plots of vertical velocity and diabatic heating averaged over the disturbance region. It is obvious that the air columns being disturbed show periodic features in all the simulations. In the CTLF10, the moist bubble triggers a burst of convection after 6 hours. From 6 h to 18 h, upward motion predominates in the free troposphere (Fig. 2a). The diabatic heating exhibits a maximum located around 4 km (Fig. 2g), which is a typical deep convective heating in TMCCs, usually referred to as the first baroclinic heating mode. Notably, the vertical velocity and diabatic heating reach their respective maxima around 12 h, aligning with the peak precipitation observed in the disturbance (Fig. 1a).

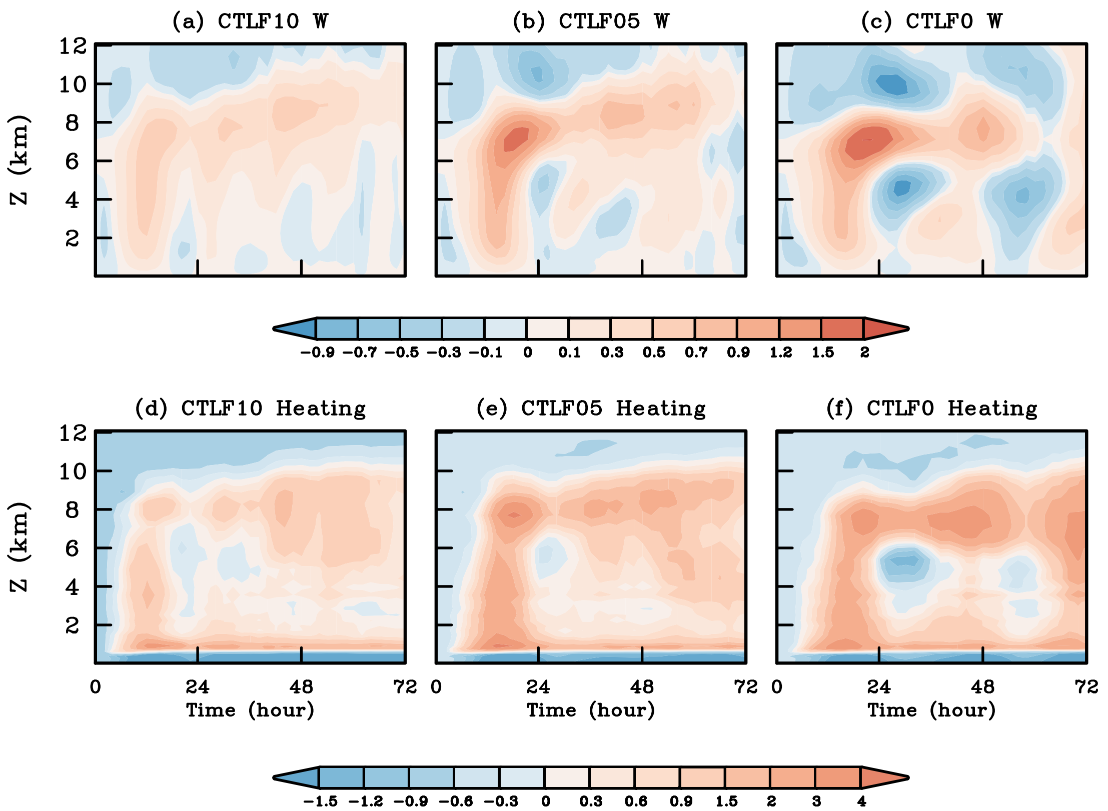

Fig. 2 The time-height plot of (a) vertical velocity (cm s^{-1}) and (d) diabatic heating (K day^{-1}), all averaged in the inner 150 km radii of the disturbance in CTLF10. (b), (e) and (c), (f) are for CTLF05 and CTLF0, respectively.

After 12 hours, the vertical velocity and diabatic heating begin to decay. A subsidence occurs from 18 hours to 24 hours, spanning from 4 km down to the surface. During this phase, the diabatic heating in the free troposphere mainly displays a wavenumber-one structure in the vertical direction, characterized by heating above 7 km and cooling below. This heating profile is typical of stratiform heating in TMCCs, often referred to as the second baroclinic heating mode. Traditionally, it is believed that stratiform precipitation is associated with downward motion and BL divergence, which typically inhibits subsequent convection at the same location (e.g., Houze 1982; Houze 2018). However, deep convection reoccurs after 24 hours, and the disturbance repeats the above cycle over the next several days (Fig. 2). A similar pattern is observed in simulations CTLF05 and CTLF0, except the period of the cycles are different (Fig. 2).

The occurrence of a periodic convection raises two critical questions: What mechanisms facilitate the recovery of deep convection after the stratiform precipitation in the disturbance air column? Additionally, what determines the period of the cycle? We will address these two questions in the next two sections.

4. Recovery of convection: the critical role of low-level buoyancy

To understand the recovery of convection after the stratiform precipitation in TMCCs, we need to understand the evolution of the critical variables that determine the precipitation. Previous studies have demonstrated that low-level buoyancy plays a crucial role in determining precipitation in TMCCs (e.g., Ahmed and Neelin 2018; Ahmed et al. 2020). Following Ahmed et al. (2020), the low-level buoyancy can be expressed as:

$$B_{low} = g\left(w_1 \frac{\theta_{eBL} - \theta^*_{elow}}{\theta^*_{elow}} - w_2 \frac{\theta^*_{elow} - \theta_{elow}}{\theta^*_{elow}}\right), \qquad (1)$$

in which θ_{eBL} is the BL averaged θ_e, θ_{elow} is the θ_e averaged in the lower troposphere, and θ^*_{elow} is the saturation θ_e in the lower troposphere. The first term on the righthand side of Eq. (1) can be approximated as the undilute plume buoyancy based on BL properties and low-level temperature, and the second term measures the influence of low-level subsaturation (entrainment). The coefficient w_1 and w_2 are the weight of the two processes, which can be expressed as:

$$w_1 = \frac{\Delta p_B}{\Delta p_{low}} \ln\left(\frac{\Delta p_B + \Delta p_{low}}{\Delta p_B}\right),$$

$$w_2 = 1 - w_1.$$

In this study, the BL and the low-level troposphere are defined as the layer below 900hPa and the layer between 900hPa and 500hPa, respectively. With this definition, w_1 and w_2 are almost the same, so we use $w_1 = w_2 = 0.5$ to calculate the low-level buoyancy. All the averaged variables in Eq. (1) are density weighted.

The time evolution of B_{low} in the 'CTL' simulations are shown in Fig. 1b. In all the three simulations, the evolution of B_{low} is in phase with precipitation in the disturbance region after 12 hours, indicating a strong correlation between B_{low} and precipitation. For comparison, plane views of B_{low} from 22 to 54 h in CTLF10 are also presented in Fig. 3. It is evident that the most significant variations in B_{low} occur in the column being disturbed, which remains almost stationary throughout the simulation. B_{low} shows an increasing trend from 22-28 h and 38-44 h, and a decreasing trend from 30-36h and 46-52h, consistent with the trend of precipitation and B_{low} shown in Fig. 1.

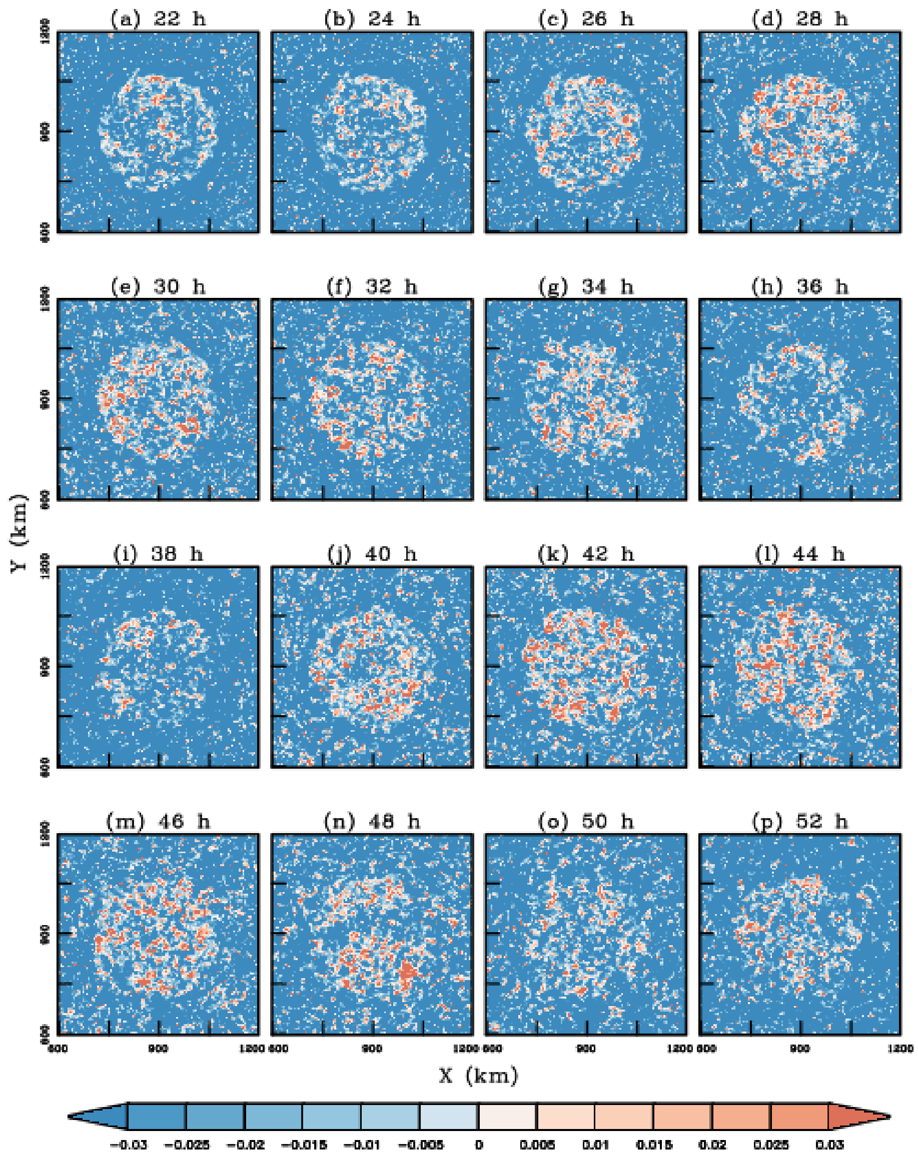

Fig. 3 Plane views of (B_{low} +0.04, m s^{-2}) from 22 h to 52 h in CTLF10. We add a constant

value of 0.04 to make the domain-mean B_{low} around 0.

To further investigate whether the evolution of B_{low} quantitatively reflects precipitation changes, we reference the findings of Ahmed et al. (2020), which establish a general precipitation increase rate of a=20 (mm h^{-1}) (m s^{-2})$^{-1}$. We apply this rate to calculate the temporal anomaly of precipitation based on the anomalies of B_{low} from 12 to 72 hours in CTLF10. As shown in Fig. 4, the precipitation anomaly estimated from B_{low} aligns closely in magnitude with the precipitation anomaly observed in the full-physics simulations. However, since the increase rate a in Ahmed et al. (2020) is estimated based on instances when B_{low} is greater than 0, as indicated by the P-B_{low} relationship (Fig. 2c in Ahmed et al. 2020), we note that a should be lower for values of B_{low} slightly below 0. We use to a=5 (mm h^{-1}) (m s^{-2})$^{-1}$ to estimate the precipitation anomaly again, and the result is almost consistent with the anomaly of precipitation in full-physics simulations (Fig. 4). This further validates that the low-level buoyancy scales well with precipitation, which can be used as a good indicator to understand the evolution of convection in TMCCs. Nonetheless, it is important to recognize that while B_{low} correlates well with precipitation, the absolute values do not always align. For instance, at 44 hours, B_{low} in CTLF0 is lower than in CTLF10, yet the precipitation in CTLF0 is greater (Fig. 1). Therefore, it is more appropriate to utilize the tendencies of B_{low} to explain changes in precipitation.

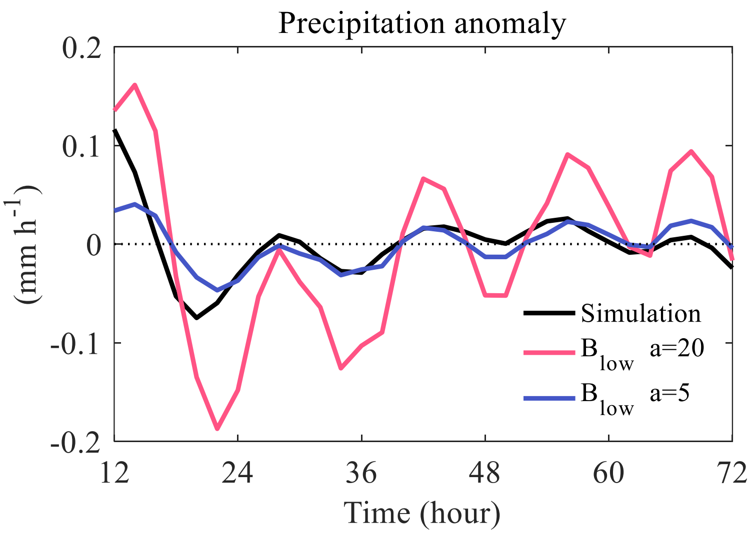

Fig.4 Time series of temporal precipitation anomaly (mm h^{-1}) from 12-72 h in the disturbance in CTLF10 (black). Red and blue lines are precipitation anomaly estimated with low-level buoyancy using coefficient *a*=20 and *a*=5, respectively.

The above analysis indicates that the recovery of low-level buoyancy is critical to the recovery of deep convection and precipitation after the stratiform heating. According to equation (1), there are three factors controlling the low-level buoyancy, which are the BL θ_e, the low-level temperature and low-level water vapor content. A higher BL θ_e, a larger low-level humidity or a lower low-level temperature will favor the increase of B_{low}. To identify which factor dominates the evolution of B_{low}, we calculate B_{low} in CTLF10 again but substitute the BL θ_e with its temporal mean from 0-72 h. Fixing the BL θ_e in Eq. (1) introduces a systematic tendency of B_{low}, while B_{low} still shows a clear oscillation (Fig. 5a). However, when the low-level temperature and moisture variation is removed using the same method, the oscillation in B_{low} diminishes (Fig. 5a). This indicates that for B_{low} to recover, it is the low levels that really matters.

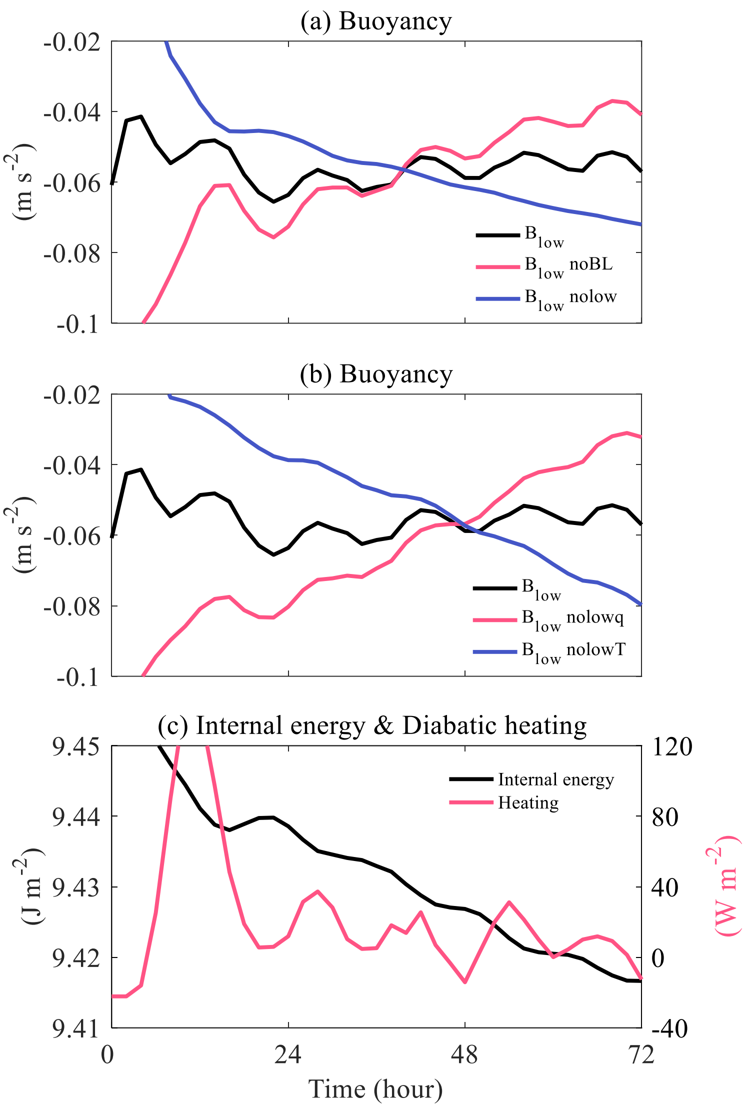

Fig.5 (a) Time series of the original B_{low} (m s^{-2}) in CTLF10 (black), B_{low} calculated with a 0-72 h temporal mean BL variables (red), and B_{low} calculated with a 0-72 h temporal mean low-level variables (blue). (b) Time series of the original B_{low} in CTLF10 (black), B_{low} calculated with a 0-72 h temporal mean low-level qv (red), and B_{low} calculated with a 0-72 h temporal mean low-level temperature (blue). (c) Time series of low-level mass-weighted internal energy (black, J m^{-2}) and diabatic heating (red, W m^{-2}).

We further investigate which characteristics of the low-level atmosphere are most significant in influencing the oscillation of B_{low}. We recalculated B_{low} in CTLF10 by substituting the temperature and water vapor with their temporal means from 0 to 72 hours, respectively. The results indicate that the oscillation of B_{low} nearly disappears when the variation in low-level temperature is eliminated (Fig. 5b). This suggests that low-level cooling is the primary factor influencing B_{low} and, in turn, precipitation

In this section, we have demonstrated that the oscillation of precipitation can be explained by the oscillation of low-level buoyancy, which is primarily influenced by variations in low-level temperature. However, the mechanisms underlying low-level cooling after stratiform heating, which is critical for the recovery of buoyancy and convection, remain unclear. Previous studies have attributed low-level cooling to the diabatic cooling associated with stratiform heating structures (e.g., Mapes 2000; Kuang 2008b). Nevertheless, Fig. 5c illustrates that low-level diabatic cooling actually corresponds to a warming process, with cooling occurring 1/4 of a period later than the diabatic cooling. This suggests that low-level cooling is not directly caused by the diabatic cooling of the stratiform heating structure; rather, it may stem from adiabatic responses triggered by this heating structure. In the following section, we will explore the occurrence of low-level cooling and the recovery of buoyancy from the perspective of adiabatic processes.

5. Recovery of Buoyancy: an inertia-gravity oscillation

In this section, we conduct a series of dry experiments termed ‘Dry2’ to investigate the recovery of buoyancy in TMCCs after stratiform heating (Table 1). These simulations have a domain size of 3000 km × 3000 km with open lateral boundary conditions. Additionally, there is no radiation or microphysics parameterization, while the other settings remain consistent with the ‘CTL’ series. The dry simulations are initialized with a stratiform heating profile, with its structure as follows:

$$Q(r,z) = \begin{cases} Q_0 \sin(2\pi z/H - \pi)\cos(\pi r/2R) & (z < H \ and \ r < R) \\ 0 & (z \geq H \ or \ r \geq R) \end{cases} \quad (2)$$

In Eq. (2), r and z represent radius and height, respectively. H and R are the maximum height and radius of the heating, which are 12 km and 150 km, respectively. Q_0 is the magnitude of the heating, which is set to be 0.001 K s^{-1}. This heating has a typical tropical stratiform heating profile in the vertical direction (Fig. 6), which decays sinusoidally with radius. In all the dry simulations, heating is maintained for two hours, followed by an additional 46 hours of simulation.

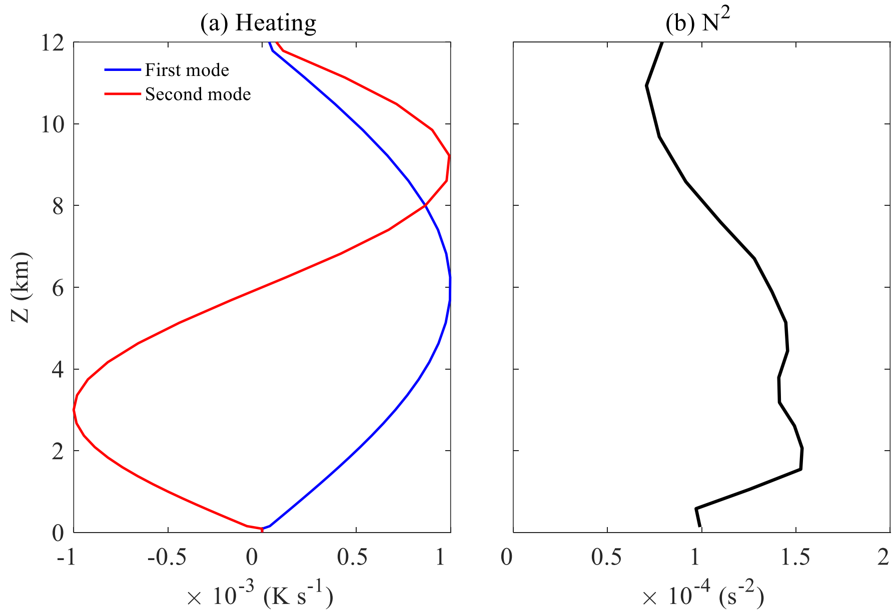

Fig. 6 Vertical profiles of (a) the first (blue) and second (red) diabatic heating (K s^{-1}) used in the dry simulations, and (b) the N^2 (s^{-2}) in the initial field.

The immediate response of the air column in Dry2_F10 to the heating is characterized by upward motion above 6 km and downward motion below 6 km (Fig. 7a). Although these vertical motions may induce adiabatic cooling at upper levels and warming at lower levels, they are insufficient to offset the diabatic heating and cooling over such a short time frame. Consequently, warm and cold anomalies develop at 9 km and 3 km, respectively, during the initial hours (Fig. 7d). Additionally, the vertical motion redistributes water vapor content (qv). Given that the qv at upper levels is minimal, the most significant change in the qv field over the first several hours is a drying tendency at lower levels. It should be noted that since Figs. 7d-f and figs. 7g-i plot the temporal anomalies of θ and qv, respectively, it is the change of the anomalies that really matters.

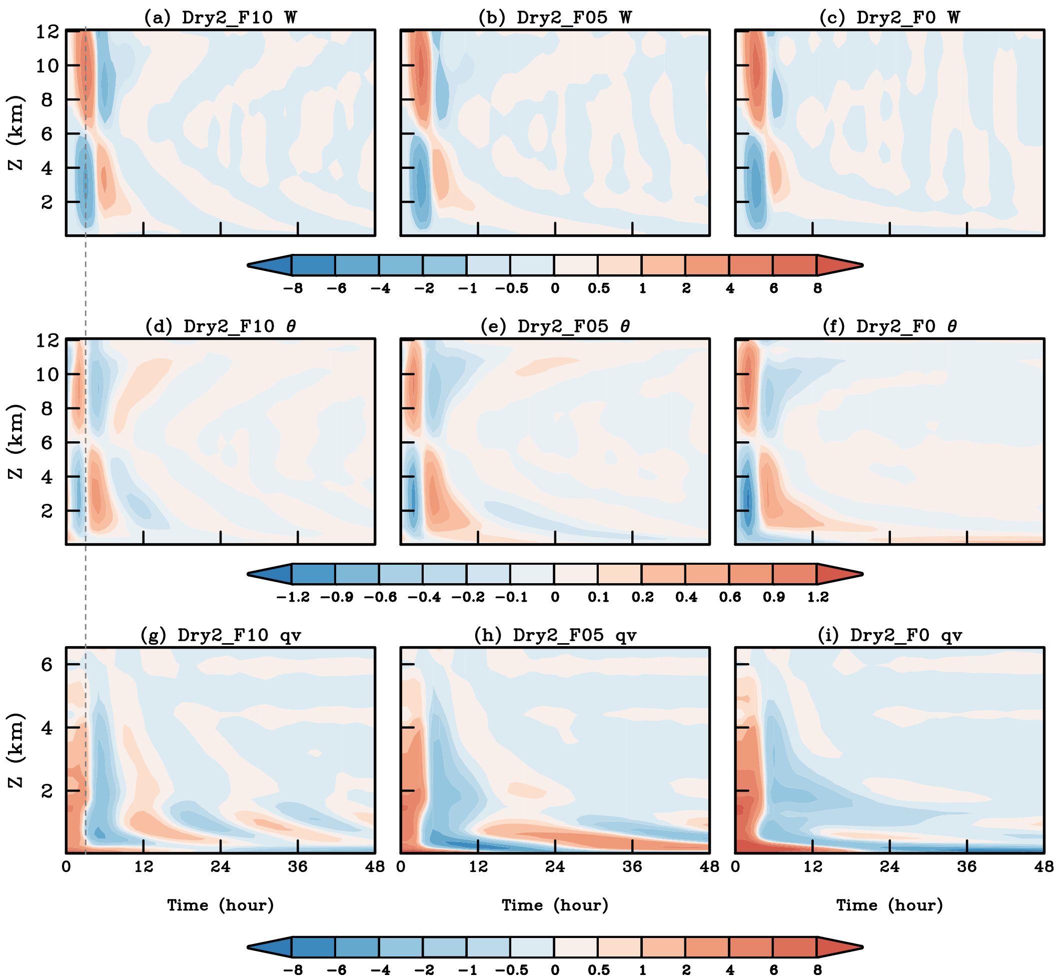

Fig. 7 The time-height plot of (a) vertical velocity (cm s^{-1}), (d) temporal potential temperature anomaly (K), and (g) temporal qv anomaly (g kg^{-1}), all averaged in the inner 150 km radii of the disturbance in Dry2_F10. (b), (e), (h) and (c), (f), (i) are for Dry2_F05 and Dry2_F0, respectively. The vertical dashed line marks the moment that the low-level vertical velocity reaches the first minimum, indicating that the temperature and qv anomaly is 1/4 period behind the vertical velocity.

Although the diabatic heating ceases after 2 hours, the response of vertical motion persists for a significantly longer duration. The evolution of temperature and qv lags the vertical velocity by one-fourth of the oscillation period, suggesting that vertical motion is the driving force behind the changes in temperature and qv. The low-level subsidence further results in warming and drying at lower levels, which decreases low-level buoyancy and hinders the occurrence of convection (Fig. 8). However, the vertical motion reverses after 6 hours, resulting in a cooler and more moist lower troposphere, which enhances B_{low} (Fig. 8). In fact, the vertical motion undergoes periodic sign changes, leading to oscillations in temperature and qv (Figs. 7a, d, & g), and, in turn, B_{low} (Fig. 8). In Dry2_F05 and Dry_F0, we also observe similar oscillations (Figs. 7 & 8). It is evident that the oscillation period increases as the Coriolis parameter decreases, which is consistent with the results observed in the full-physics simulations (Fig. 2). It is important to note that in all the dry simulations, the oscillation period varies with altitude (Fig. 7). The profile of the period generally exhibits a 'C' shape (Fig. 9), characterized by shorter periods at middle levels and longer periods at both upper and lower altitudes (the period is defined as the first return period of the vertical velocity maximum above 6 km, and the first return period of the vertical velocity minimum below 6 km). This pattern leads to an increase in vertical wavenumber over time (Fig. 7).

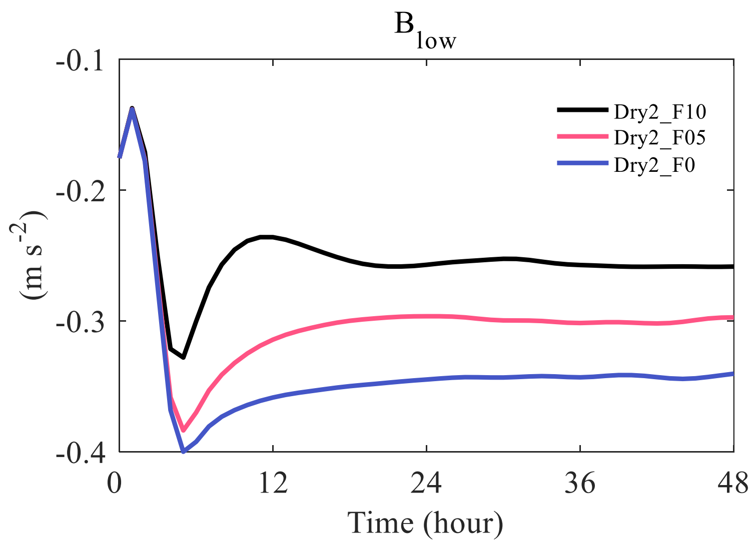

Fig. 8 Time series of B_{low} (m s^{-2}) in Dry2_F10 (black), Dry2_F05 (red), and Dry2_F0 (blue).

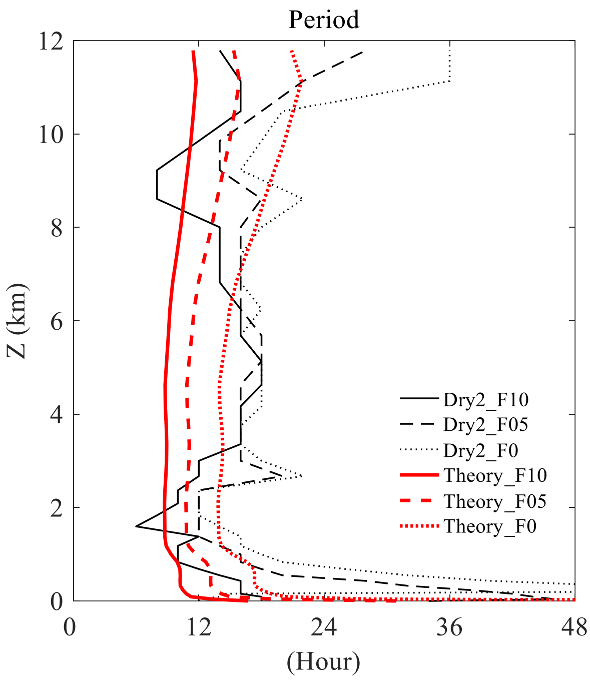

Fig. 9 Vertical profiles of period (hour) in Dry2_F10 (black solid), Dry2_F05 (black dashed) and Dry2_F0 (black dotted). Red lines are their counterparts estimated by the linear theory.

Now we have shown that even in dry simulations, an air column perturbed by a stratiform heating profile exhibits internal oscillations, which contribute to the recovery of low-level buoyancy that supports subsequent episodes of convection. Given that the simulations are conducted on an f-plane within a stratified atmosphere, these oscillations are likely inertia-gravity oscillations. In the following part of this section, we will validate this inertia-gravity nature by comparing the characteristics of these oscillations with established theoretical frameworks.

If an air column is undergoing inertia-gravity oscillations, it will generate inertia-gravity waves characterized by specific structures. We begin by comparing the characteristics of the dry waves with inertia-gravity wave theories as described in textbooks. The radius-height structures of several key variables outside the disturbance region in Dry2_F10, as shown in Fig. 10, indicate an outward propagating wave signal. The first wave front exhibits subsidence at upper levels and ascent at lower levels, resulting in respective warm and cold anomalies occurring one-fourth of a wavelength behind the vertical motion (Figs. 10a, d & g). This structure aligns with findings from previous studies (e.g., Nicholls et al. 1991; Mapes 1993).

According to linear inertia-gravity wave theory, when the phase line of the cold anomaly is situated above the warm anomaly, an ascent motion and outward radial velocity anomaly should exist between them (Fig. 5.12, Holton and Hakim 2012). The left and middle columns in Fig. 10 illustrate that the relationships between temperature and vertical and radial velocity are consistent with this theoretical expectation. Furthermore, theory predicts that tangential velocity maxima should occur where the radial velocity changes sign. As depicted in the right column of Fig. 10, similar phenomena are observed. The alignment of the wave structure with textbook theory reinforces the conclusion that these waves are inertia-gravity waves, indicating that the air column is undergoing inertia-gravity oscillations.

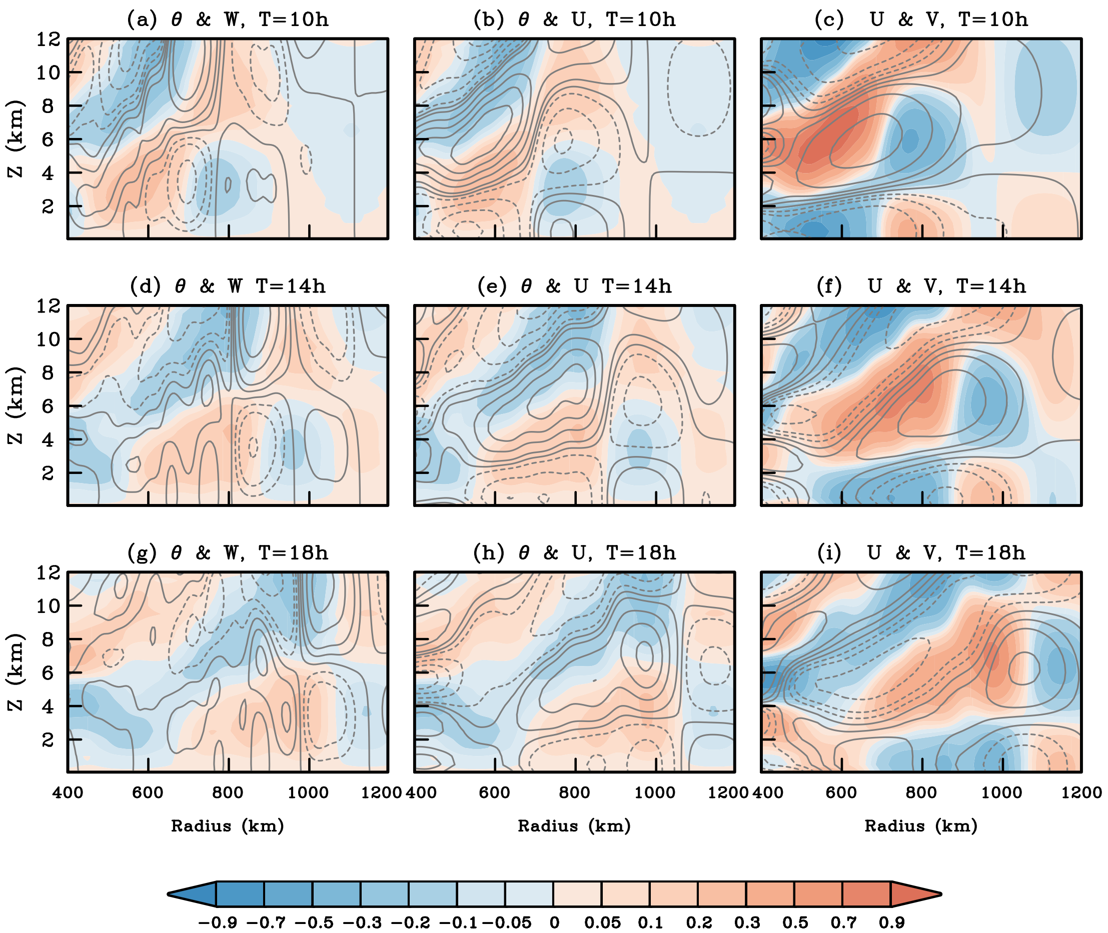

Fig. 10 Radius-height plots of azimuthal-mean of (a) horizontal potential temperature

anomaly (K, shading) and vertical velocity (contour at -3, -2, -1, -0.5, 0, 0.5, 1, 2 and 3 cm s^{-1}), (b) horizontal potential temperature anomaly (K, shading) and radial velocity (contour at 0.9, -0.7, -0.5, -0.3, -0.1, 0, 0.1, 0.3, 0.5, 0.7 and 0.9 m s^{-1}), and (c) radial velocity (cm s^{-1}, shading) and tangential velocity (contour at -0.6, -0.4, -0.2, -0.1, -0.05, 0, 0.05, 0.1, 0.2, 0.4 and 0.6 m s^{-1}). The upper, middle and lower panel are for 10 h, 14 h and 18 h in Dry2_F10, respectively.

In comparison, we present the radius-height plots of the same variables from the full-physics simulation CTLF10 (Fig. 11). Due to a systematic warming tendency above 7 km, which may obscure the wave signal, we focus only on the structures below 6 km. In CTLF10, diabatic heating is a composite of shallow convective, deep convective, and stratiform heating processes. As a result, the wave structures are not as clearly defined as those in the dry simulations. Nevertheless, several dominant features of inertia-gravity waves remain evident. For instance, we observe that downward (upward) motion consistently precedes the warm (cold) anomaly, the phase lines separating the cold and warm anomalies align with the radial velocity, and the tangential velocity maxima correspond to points where the radial velocity changes sign. These observations suggest that even in full-physics simulations, the oscillation generally retains its inertia-gravity characteristics.

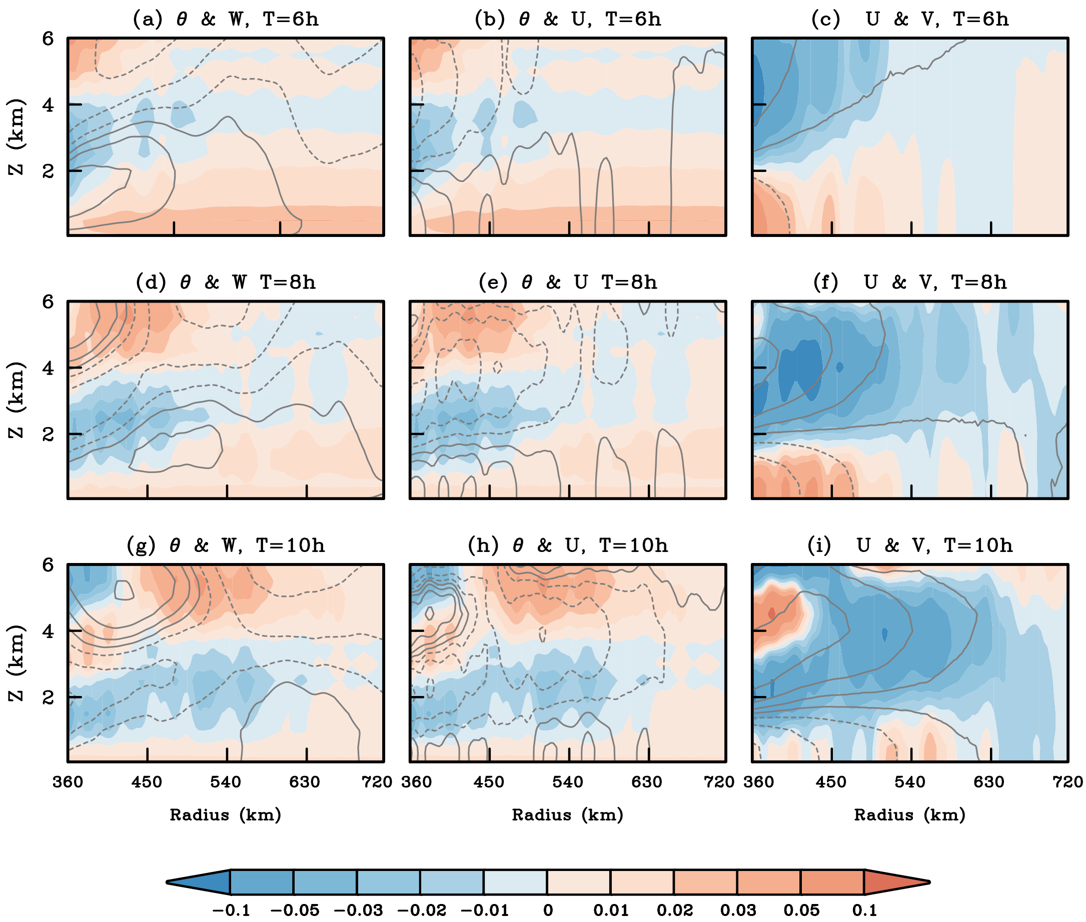

Fig. 11 As in Fig.9, but for CTLF10 at 6 h (upper) 8 h (middle) and 10 h (lower).

While the structure of the wave aligns with inertia-gravity wave theory, more quantitative evidence would come from consistency in the dispersion relationship. According to the linear inertia-gravity wave theories, the frequency of the oscillation can be estimated with the properties of the wave, which can be written as:

$$\nu^2 = f^2 + N^2(k^2 + l^2)m^{-2} \quad (3)$$

In Eq. (3), ν is the frequency of the oscillation, f is the Coriolis parameter and N^2 is the frequency. k and l are the respective wavenumber in the x and y direction, and k^2+l^2 is thus the square of the wavenumber in the radial direction. m is the wavenumber in the vertical direction.

Since we have applied a stratiform heating structure in the disturbance as shown in Fig. 6a, the wavelength in the vertical direction should be 12 km. Potential temperature, vertical motion, and radial velocity exhibit a wavelength of around 600 km (Fig. 10).

However, the tangential velocity displays a longer wavelength, with a wavelength exceeding 400 km (Figs. 10f & h). For simplification, we assume a general wavelength of 750 km, which is roughly five times the size of the disturbance. By substituting the profile of N^2 shown in Fig. 6b, we can estimate the oscillation period using Eq. (3). The estimated oscillation period aligns closely with the results from Dry2_F10 (Fig. 9) and exhibits a 'C' shape in the vertical direction, attributed to smaller values of N^2 at both upper and lower altitudes. Furthermore, the wavelengths in Dry2_F05 and Dry2_F0 are slightly longer compared to those in Dry2_F10 (Figs. 12b & c). We estimate the general wavelengths in Dry2_F05 and Dry2_F10 to be 900 km and 1050 km, respectively, and the estimated periods are also consistent with those observed in the dry simulations (Fig. 9).

From the dispersion relationship, we can also infer the phase speed of the wave. The phase speed is written as:

$$c = \nu \Big/ \sqrt{k^2 + l^2} \,. \tag{4}$$

We substituted the respective periods and wavelength of Dry2_F10, Dry2_F05, and Dry2_F0 at a height of 3 km (10, 15, and 18 hours, respectively, as shown in Fig. 11) into Eq. (4). This yielded theoretical phase speeds of 20.8 m/s, 16.7 m/s, and 16.2 m/s, respectively. As illustrated in Figs. 12a-c, the phase speeds of the first wave bore in Dry2_F10, Dry2_F05, and Dry2_F0 are 22.4 m/s, 20.8 m/s, and 18.2 m/s, respectively. Overall, the theoretical phase speeds are close to those observed in the dry simulations, and they both show an increase in phase speed with a larger Coriolis parameter.

From the analysis presented above, it is evident that the periods and wave speeds estimated from the theory generally align with the results observed in the dry simulations, confirming that the oscillation is an inertia-gravity oscillation.

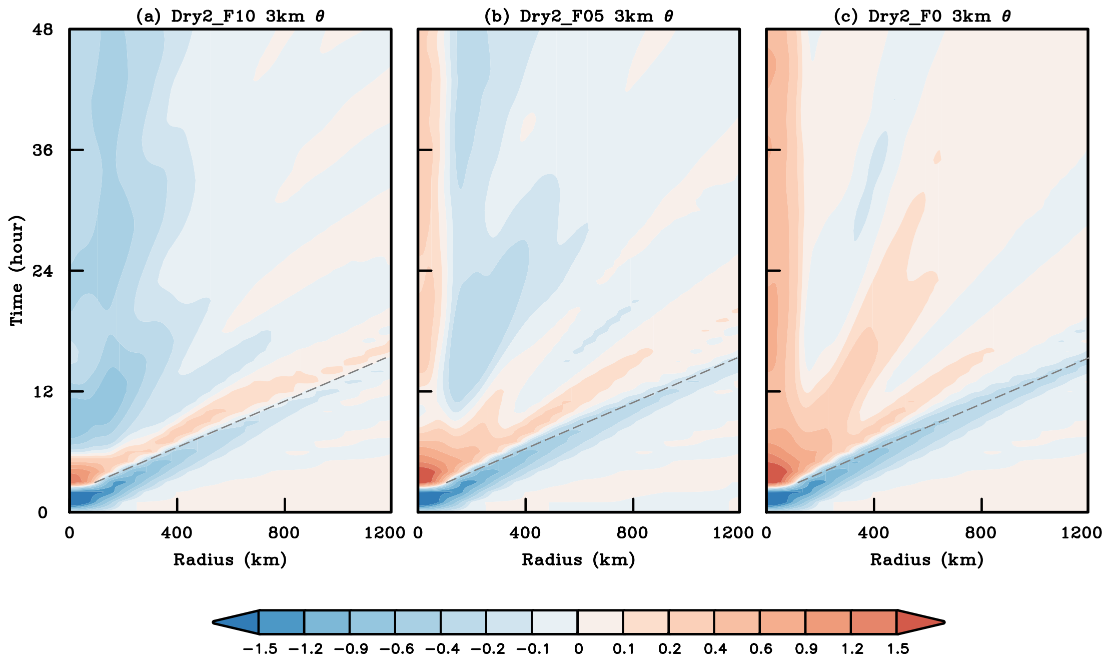

Fig. 12 Radius–time Hovmöller diagram of the azimuthal-mean of horizontal potential temperature anomaly (K) at 3 km height in (a) Dry2_F10, (b) Dry2_F05 and (c) Dry2_F0. The dashed line shows the phase line where potential temperature anomaly changes sign in Dry2_F10.

Finally, we examine the response of the dry atmosphere to the first baroclinic heating mode, as this heating mode is also a dominant feature in TMCCs. The set of ‘Dry1’ simulations is designed similarly to the ‘Dry2’ simulations (Table 1), with the only difference being the application of the first baroclinic heating mode in the vertical direction (Fig. 6a). Upon model initialization, the deep heating triggers upward motion throughout the entire column (Figs. 13a-c). Although this upward motion induces adiabatic cooling, it is insufficient to counterbalance the diabatic heating, resulting in warming across the entire column during the first 2 hours (Figs. 13d-f). After the heating ceases, the upward motion continues for a longer duration, leading to cooling and moistening of the lower atmosphere. This phenomenon may help to invigorate deep convection and prolong the presence of the first heating mode observed in full-physics simulations. After 6 hours, the vertical velocity becomes negative in the disturbance region (Figs. 13a-c), which reduces the cold and wet anomalies in the column (Figs. 13d-i). However, there is no clear recovery of upward motion or low-level buoyancy following this period, nor is there any indication of oscillation. Furthermore, the magnitude of the response in the ‘Dry1’ simulations is significantly smaller compared to that in the ‘Dry2’ simulations. These results strongly suggest that it is the second baroclinic heating mode that is responsible for the inertia-gravity oscillation.

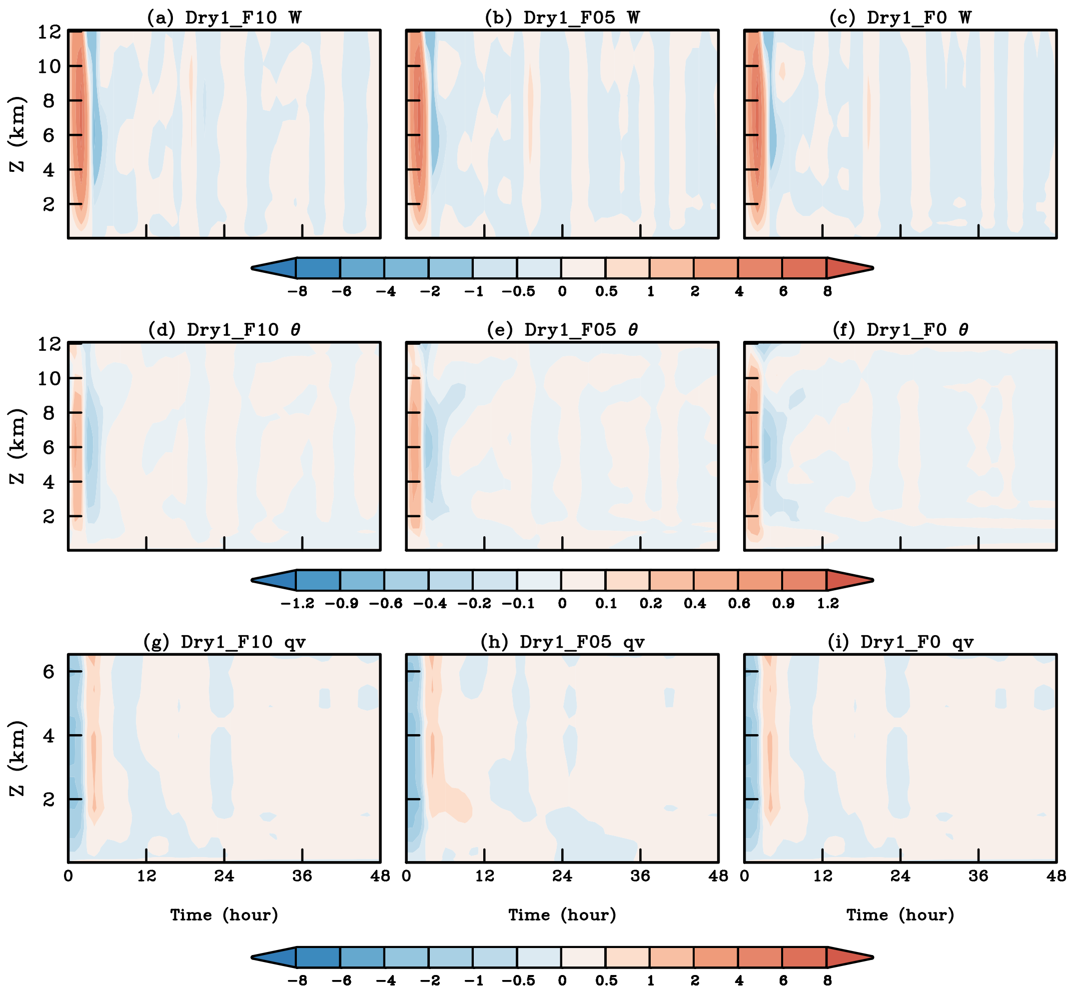

Fig. 13 As in Fig. 6, but for Dry1_F10, Dry1_F05 and Dry1_F0.

From the dry simulations in this section, we have demonstrated that the stratiform heating profile is critical to the recovery of low-level buoyancy. Although the immediate response of low-level stratiform cooling does not favor buoyancy recovery, the inertia-gravity oscillation triggered by the stratiform heating soon results in ascent at the lower levels of the column. This upward motion cools and moistens the lower atmosphere, leading to the recovery of low-level buoyancy and, consequently, a new episode of deep convection.

6. Discussion and Summary

The interaction between convective clusters and waves has been a prominent topic of research for decades. Previous studies often treat waves as large-scale external forcings, and have gained a lot of understanding on how these waves may modulate convective clusters. However, most of these studies do not address the feedback from convective clusters to the waves. How the convective clusters influence the wave, and in turn, the cluster themselves, remains unclear. A handful of studies (e.g., Kuang 2008a; Kuang 2010; Tulich and Mapes, 2010) have investigated the response of convective heating to the waves. However, these studies either treated the entire simulation domain as the disturbance or use parameterizations to represent the large-scale response, both of which limit their ability to directly resolve the interactions between the disturbance and the environment.

In this study, we directly simulate the interaction between a mesoscale disturbance and its environment. It is demonstrated that tropical mesoscale convective clusters exhibit internal oscillations, significantly influenced by the oscillation (wave) they generate themselves. When deep convection within a cluster decays, the system becomes dominated by the stratiform heating profile. This stratiform heating facilitates the recovery of buoyancy and initiates new convection by triggering an inertia-gravity oscillation. As the new convection decays, stratiform heating occurs again, leading to another oscillation, and this cycle continues. In contrast to previous studies, the diabatic heating in this oscillation is not solely a consequence of the preceding oscillation; it also serves as the source for the subsequent oscillation. The wave source (heating) is renewed with each oscillation period, establishing this as a convectively coupled inertia-gravity oscillation.

Two key points are highlighted through this research. The first is the critical role of low-level buoyancy. In many previous studies, the latent heat release in convective clusters is often linked to BL convergence. This concept has been incorporated into many cumulus parameterizations (e.g., Hayashi and Sumi 1986; Lau and Peng1987), but sometimes lead to unstable growth at the finest grid scales, resulting in the blow up of simulations (CISK catastrophe, e.g., Crum and Dunkerton 1992; Matthews and Lander 1999). Recent studies by Liu et al. (2019, 2022) proposed that latent heat release actually lags behind BL convergence. Cumulus parameterizations accounting for this time lag yield significantly better performance. Our study indicates that the variability of precipitation in a TMCC is not controlled by changes in the BL, but rather dominated by variations in low-level buoyancy, which are mainly influenced by changes in low-level temperature. The time lag identified by Liu et al. (2019, 2022) actually represents the time required for the system to transition from a low-level vertical velocity maximum to a temperature minimum, approximately one-fourth of the oscillation period (Fig. 7). Recognizing the critical role of low-level buoyancy in precipitation dynamics provides valuable insights for improving cumulus parameterizations from the 'wave-CISK' perspective.

Another important point to mention is the critical role of stratiform heating. Although stratiform heating initially leads to subsidence and a reduction in buoyancy, which does not favor deep convection, it soon results in upward motion and a recovery of buoyancy that triggers the next episode of convection. Compared to deep convective heating, stratiform heating is more effective in inducing oscillation. This efficiency arises from the larger vertical wavenumber associated with stratiform heating, which results in slower outward propagation of energy, allowing more energy to remain available for maintaining the oscillation of the air column (e.g., Wu 2000; 2003). In real-world scenarios, stratiform heating is typically much weaker than deep convective heating, making the oscillation susceptible to contamination and influence from other signals, such as large-scale waves and the diurnal cycle of insolation. Therefore, TMCCs with stronger intensity will be easier to sustain a quasi-periodic oscillation. In a companion paper, we will demonstrate that this quasi-periodic oscillation does occur in tropical cyclone precursors.

In fact, the internal oscillation identified in this study offers a new perspective for understanding and predicting the variations of TMCCs in the real world. With the demonstration of internal oscillation, the first-order interaction between TMCCs and other periodic forcings can be simplified to the overlapping of two (or more) sinusoidal signals with differing periods. This approach provides clearer physical intuition for comprehending the variation of TMCCs in real-world scenarios. As an example, we will illustrate in a companion paper that the phase synchronization of the internal oscillation of a TC precursor with the diurnal cycle of insolation can systematically enhance convective activity, ultimately accelerating TC genesis. However, an urgent question that needs to be addressed is the identification of factors influencing the oscillation period. This study indicates that, in addition to the Coriolis parameter and stratification, a significant influence may arise from the coupling of convection. When coupled with convection, the recovery of deep convection occurs more swiftly than in dry cases, particularly when the Coriolis parameter is smaller. The interplay of convection complicates the processes, resulting in a complex area that necessitates further investigation.

Acknowledgement

This work is jointly supported by the National Natural Science Foundation of China 42205004, the China Postdoctoral Science Foundation 2024T170011 and the China Scholarship Grant 202406010151.

Reference

1. Ahmed, F., and J. D. Neelin, 2018: Reverse engineering the tropical precipitation–buoyancy relationship. *J. Atmos. Sci.*, **75**, 1587-1608.
2. Ahmed, F., Á. F. Adames, and J. D. Neelin, 2020: Deep Convective Adjustment of Temperature and Moisture. *J. Atmos. Sci.*, **77**, 2163–2186.
3. Browner, S. P., W. L. Woodley, and C. G. Griffith, 1977: Diurnal oscillation of the area of cloudiness associated with tropical storms. *Mon. Wea. Rev.*, **105(7)**, 856–864.
4. Crum, F. X., and T. J. Dunkerton, 1992: Analytic and numerical models of wave–CISK with conditional heating. *J. Atmos. Sci.*, **49**, 1693–1708.
5. Diaz, M., and W. R. Boos, 2021a: Evolution of idealized vortices in monsoon-like shears: Application to monsoon depressions. *J. Atmos. Sci.*, **78**, 1207–1225.
6. Diaz, M., and W. R. Boos, 2021b: The influence of surface heat fluxes on the growth of idealized monsoon depressions. *J. Atmos. Sci.*, **78**, 2013–2027.
7. Dunion, J. P., C. D. Thorncroft, and C. S. Velden, 2014: The Tropical Cyclone Diurnal Cycle of Mature Hurricanes. *Mon. Wea. Rev.*, **142**, 3900–3919.
8. Emanuel, K., 2018: 100 years of progress in tropical cyclone research. *Meteorol. Monogr.*, **59**, 11–15.
9. Fingerhut, W. A., 1978: A Numerical Model of a Diurnally Varying Tropical Cloud Cluster Disturbance. *Mon. Wea. Rev.*, **106**, 255–264.
10. Gray, W. M., and R. W. Jacobson Jr., 1977: Diurnal variation of deep cumulus convection. *Mon. Wea. Rev.*, **105**, 1171–1188.
11. Haertel, P. T., and R. H. Johnson, 1998: Two-day disturbances in the equatorial western Pacific. *Quart. J. Roy. Meteor. Soc.*, **124**, 615 636.
12. Haertel, P. T., and G.N. Kiladis, 2004: Dynamics of 2-day equatorial waves. *J. Atmos. Sci.*, **61**, 2707–2721.
13. Hayashi, Y., and A. Sumi, 1986: The 30–40 day oscillations simulated in an ‘‘aqua-planet’’ model. *J. Meteor. Soc. Japan*, **64**, 451–467.
14. Holton, B. J. R. and G. J. Hakim, 2012: An Introduction to Dynamic Meteorology.

5th ed. Academic Press, 535 pp.

15. Hong, S. Y., Y. Noh, and J. Dudhia, 2006: A new vertical diffusion package with an explicit treatment of entrainment processes. *Mon. Wea. Rev.*, **134**, 2318–234.
16. Houze, R. A., 1982: Cloud clusters and large-scale vertical motions in the tropics. J. Meteor. Soc. Japan, 60, 396–410
17. Houze, R. A., 2018: 100 Years of Research on Mesoscale Convective Systems. *Meteor. Monogr.*, **59**, 17.1–17.54.
18. Iacono, M. J., J. S. Delamere, E. J. Mlawer, M. W. Shephard, S. A. Clough, and W. D. Collins, 2008: Radiative forcing by long-lived greenhouse gases: Calculations with the AER radiative transfer models. *J. Geophys. Res*., **113**, D13103.
19. Jordan, C. L., 1958: Mean soundings for the West Indies area. *J. Meteor.*, **15**, 91–97.
20. Kuang, Z., 2008: A moisture-stratiform instability for convectively coupled waves. *J. Atmos. Sci.*, **65**, 834–854.
21. Kuang, Z., 2010: Linear Response Functions of a Cumulus Ensemble to Temperature and Moisture Perturbations and Implications for the Dynamics of Convectively Coupled Waves. *J. Atmos. Sci.*, **67**, 941–962.
22. Lau, K., and L. Peng, 1987: Origin of Low-Frequency (Intraseasonal) Oscillations in the Tropical Atmosphere. Part I: Basic Theory. *J. Atmos. Sci.*, **44**, 950–972
23. Li, T., X. Ge and B. Wang, 2006: Tropical cyclogenesis associated with Rossby wave energy dispersion of a preexisting typhoon. Part II: Numerical simulations. *J. Atmos. Sci.*, **63**, 1390–1409.
24. Liu, Y., Z. Tan, and Z. Wu, 2019: Noninstantaneous wave-CISK for the interaction between convective heating and low-level moisture convergence in the tropics. J. *Atmos. Sci.*, **76**, 2083–2101.
25. Liu, Y., Z. Tan, and Z. Wu, 2022: Convective Response in a Cloud-Permitting Simulation of the MJO: Time Scales and Processes. *J. Atmos. Sci.*, **79**, 1473–1490.
26. Matthews, A. J., and J. Lander, 1999: Physical and numerical contributions to the structure of Kelvin wave-CISK modes in a spectral transform model. *J. Atmos. Sci.*,

56, 4050–4058.

27. Mapes, B. E., 1993: Gregarious Tropical Convection. *J. Atmos. Sci.*, **50**, 2026–2037.
28. Mapes, B. E., 2000: Convective inhibition, subgrid-scale triggering energy, and stratiform instability in a toy tropical wave model. *J. Atmos. Sci.*, **57**, 1515–1535.
29. Nesbitt, S. W., E. J. Zipser, and D. J. Cecil, 2000: A census of precipitation features in the tropics using TRMM: Radar, ice scattering, and lightning observations. *J. Climate*, **13**, 4087-4106.
30. Nicholls, M. E., R. A. Pielke, and W. R. Cotton, 1991: Thermally Forced Gravity Waves in an Atmosphere at Rest. *J. Atmos. Sci.*, **48**, 1869–1884.
31. Nicholls, M. E., and M. Montgomery, 2013: An examination of two pathways to tropical cyclogenesis occurring in idealized simulations with a cloud-resolving numerical model. *Atmos. Chem. Phys.*, **13**, 5999–6022.
32. Nicholls, M. E., 2015: An investigation of how radiation may cause accelerated rates of tropical cyclogenesis and diurnal cycles of convective activity. *Atmos. Chem. Phys.*, **15**, 9003–9029.
33. Nolan, D. S., 2007: What is the trigger for tropical cyclogenesis? *Aust. Meteor. Mag.*, **56**, 241–266.
34. Skamarock, W. C., Klemp, J. B., Dudhia, J., Gill, D. O., Liu, Z., Berner, J., Wang, W., Powers, J. G., Duda, M. G., Barker, D. M., and Huang, X.-Y. (2019), A Description of the Advanced Research WRF Model Version 4, UCAR/NCAR, https://doi.org/10.5065/1DFH-6P97.
35. Takayabu, Y. N., 1994: Large-scale cloud disturbances associated with equa torial waves. Part II: Westward-propagating inertio-gravity waves. *J. Meteor. Soc. Japan*, **72**, 451–465.
36. Takayabu, Y. N., K. M. Lau, and C. H. Sui, 1996: Observation of a quasi-2-day wave during TOGA COARE. *Mon. Wea. Rev.*, **124**, 1892–1913.
37. Thompson, G., R. M. Rasmussen, and K. Manning, 2004: Explicit forecasts of winter precipitation using an improved bulk microphysics scheme. Part I: Description and sensitivity analysis. *Mon. Wea. Rev.*, **132**, 519–542.

38. Tulich, S. N., and B. E. Mapes, 2010: Transient environmental sensitivities of explicitly simulated tropical convection. *J. Atmos. Sci.*, **67**, 923–940.

39. Wheeler, M., and G. N. Kiladis, and P. J. Webster, 2000: Large-scale dynamical fields associated with convectively coupled equatorial waves. *J. Atmos. Sci.*, **57**, 613–639.

40. Wu, Q., Ruan, Z., Chen, D. and Lian, T., 2015: Diurnal variations of tropical cyclone precipitation in the inner and outer rainbands. *J. Geophys. Res.*, **120**, 1–11.

41. Wu, Z., E. S. Sarachik, and D. S. Battisti, 2000b: Vertical structure of convective heating and the three-dimensional structure of the forced circulation on an equatorial beta plane. *J. Atmos. Sci.*, **57**, 2169–2187.

42. Wu, Z., 2003: A shallow CISK, deep equilibrium mechanism for the interaction between large-scale convection and large-scale circulations in the tropics. *J. Atmos. Sci.*, **60**, 377–392.

43. Yang, B., and Z.-M. Tan, 2020: Interactive radiation accelerates the intensification of the midlevel vortex for tropical cyclogenesis. *J. Atmos. Sci.*, **77**, 4051–4065.